

Accepted by AJ. Full version including Figure 1 at  
<http://aries.phys.yorku.ca/~ovidiu/Paper3.ps.gz> (5 MB)

## Infrared Properties of Star Forming Dwarf Galaxies: II. Blue Compact Dwarf Galaxies in the Virgo Cluster<sup>1</sup>

Vaduvescu, Ovidiu

*York University, Department of Physics and Astronomy  
 4700 Keele Street, M3J 1P3, Toronto, ON, Canada  
 email: ovidiu@yorku.ca*

Richer, Michael G.

*Observatorio Astronomico Nacional, Instituto de Astronomia, UNAM,  
 PO Box 439027, San Diego, CA 92143-9027, USA  
 email: richer@astrosen.unam.mx*

McCall, Marshall L.

*York University, Department of Physics and Astronomy  
 4700 Keele Street, M3J 1P3, Toronto, ON, Canada  
 email: mccall@yorku.ca*

### ABSTRACT

A sample of 16 blue compact dwarf galaxies (BCDs) in the Virgo Cluster has been imaged in the near-infrared (NIR) in  $J$  and  $K_s$  on the 2.1m telescope at OAN-SPM in Mexico. Isophotes as faint as  $\mu_J = 24$  mag arcsec<sup>-2</sup> and  $\mu_{K_s} = 23$  mag arcsec<sup>-2</sup> have been reached in most of the targets. Surface brightness profiles can be fitted across the whole range of radii by the sum of two components: a hyperbolic secant (sech) function, which is known to fit the light profiles of dIs, and a Gaussian component, which quantifies the starburst near the centre. Isophotal and total fitted NIR magnitudes have been calculated, along with semimajor axes at  $\mu_J = 23$  mag arcsec<sup>-2</sup> and  $\mu_{K_s} = 22$  mag arcsec<sup>-2</sup>. The diffuse underlying component and the young starburst have been quantified using the profile fitting. Most color profiles show a constant color, between  $J - K_s = 0.7$  to 0.9 mag. The diffuse component represents the overwhelming majority of the NIR light for most BCDs, the starburst enhancing the flux by less than about 0.3 mag. Linear correlations were found between the sech scale length and the

sech magnitude, and between the sech semimajor axis and the sech magnitude. Overall, galaxies with more luminous diffuse components are larger and brighter in the centre. The central burst correlates with the diffuse component, with brighter BCDs having stronger star-bursts, suggesting that more massive objects are forming stars more efficiently. BCDs lie on the “fundamental plane” defined by dwarf irregulars (dISs) in Paper I, following the same relation between sech absolute magnitude, sech central surface brightness, and the hydrogen line-width  $W_{20}$ , although the scatter is larger than for the dIs. On the other hand, correlations between the sech absolute magnitude and the sech central surface brightness in  $K_s$  for BCDs and dIs are equally good, indicating that BCD line widths may be enhanced by turbulence or winds.

*Subject headings:* galaxies: blue compact dwarfs; near-infrared; surface brightness profiles; direct imaging; photometry;

## 1. Introduction

According to Kunth & Ostlin (2000), the concept of “compact galaxies” was introduced by Zwicky (1965), in order to refer to galaxies barely distinguishable from stars on the Palomar Sky Survey plates. In a subsequent paper, Zwicky (1970) refined the definition of a “compact galaxy” to be any galaxy (or part of a galaxy) whose surface brightness is brighter than  $20 \text{ mag arcsec}^{-2}$  in any chosen wavelength range (De Paz, Madore and Pevunova 2003). The term “blue”, as used by Zwicky (1970), refers to those galaxies satisfying the previous condition on both blue and red plates (Zwicky & Zwicky 1971). Later on, Thuan & Martin (1981) introduced the term “blue compact dwarf” (BCD) referring to those compact galaxies characterized by three main properties: low luminosity ( $M_B \gtrsim -18$ ), small sizes (diameters less than 1 kpc), and strong narrow emission lines superposed on a nearly flat continuum, similar to HII regions in spiral galaxies. As their name suggests, the visible colors of BCDs appear to be blue. The star forming rates in BCDs are huge in comparison with those in dIs (between  $0.1$  and  $1 M_\odot \text{ yr}^{-1}$ , e.g. Fanelli, O’Connell and Thuan 1988), and metallicities are low (oxygen abundance between  $Z_\odot/50$  and  $Z_\odot/2$ , e.g. Kunth & Ostlin 2000), suggesting young chemical ages.

Thuan & Martin (1981) undertook the first systematic approach to study BCDs, observing HI fluxes for a large sample (115 targets) for which they derived HI profiles, neutral

---

<sup>1</sup>These data were acquired at the Observatorio Astronomico Nacional in San Pedro Martir, Mexico.

hydrogen masses and total masses. Using the IRTF 3m telescope, Thuan (1983) observed in the near-infrared (NIR) a smaller BCD sample (36 targets), deriving a color-metallicity relation and a well defined color-luminosity relation which suggested that star formation processes are intimately linked to total masses.

James (1994) pioneered NIR surface photometry, observing 13 dwarfs in Virgo including a few BCDs. The author concluded that the NIR colours of the BCDs are paradoxically red, possibly indicating an intermediate-age stellar population. No simple evolutionary link between BCDs, dIs and dEs in the sample could be discerned.

Using a 3-component decomposition scheme applied to the surface brightness profiles of 12 BCDs, Papaderos et al. (1996) found that the size and luminosity of the purported starburst component depends upon the luminosity of the underlying component, as well as on the HI mass of the BCD. Comparing the structural properties of BCDs with those of other types of dwarfs, the authors found that for the same  $B$  luminosity, the underlying component of a BCD has a central brightness brighter by  $\sim 1.5$  mag and an exponential scale length smaller by a factor of  $\sim 2$  than that of dIs and dEs.

Employing some larger samples, other authors have derived total magnitudes, surface brightness profiles and profile decompositions in the visible (Doublier et al. 1997; Doublier, Caulet, & Comte 1999; Cairos et al. 2001) and more recently in the NIR (Boselli et al. 1997; Gavazzi, et al. 2000; Cairos et al. 2003; Noeske et al. 2003, 2004). Based upon a small sample (12 targets) observed in the NIR, Doublier, Caulet, & Comte (2001) found a systematic excess of light in the  $K$  band with respect to  $H$  and  $J$  and their previous observations in the visible, indicating that a stellar population of red giants dominates the flux. Moreover, comparisons of the metallicity-color relations of BCDs and globular clusters show very little difference, indicating that BCDs are most probably old, in contradiction with previous results. Employing a small sample (9 targets) observed in the NIR, Cairos et al. (2003) found that the morphology of BCDs is basically the same as in the optical.

Using HST and ground-based optical and NIR data, Papaderos et al. (2002) investigated I Zw 18, known to be the least chemically evolved star-forming BCD galaxy in the local Universe, with an oxygen abundance of  $12 + \log(\text{O}/\text{H}) \sim 7.2$ , or  $1/50$  of the Sun (Searle & Sargent 1972; Izotov & Thuan 1999; Kunth & Ostlin 2000). In the optical, its exponential profile is not due to an evolved stellar disc underlying its star-formation regions, but rather, due to extended ionized gas emission. The unresolved stellar component, though very compact, is not exceptional with respect to structural properties for intrinsically faint dwarfs. However, it differs strikingly from the red low surface brightness host of standard BCDs. Also, unlike more evolved BCDs, the stellar component of I Zw 18 is much more compact than the ionized gas envelope.

Despite three decades of study at various wavelengths, at least two basic questions remain open about BCDs, namely their ages and possible evolutionary links between BCDs, dIs and dEs. In particular, how to decouple the diffuse underlying component from the young starburst regions remains a fundamental problem in studying dwarf galaxies. The solution is easier to achieve in the NIR, which has the advantage of better tracing the diffuse component of BCDs, whose flux in the visible is overwhelmed by young starbursts.

About four years ago we started a long-term research programme to investigate the NIR properties of dIs and BCDs (Vaduvescu 2005). The first paper of this study, hereafter Paper I, addressed the dIs (Vaduvescu et al. 2005). Based upon deep data derived from a sample of 34 field dIs observed at CFHT, we have recently found an universal law fitting their NIR surface brightness profiles. We also found that these data permit the definition of a fundamental plane for the dIs (Paper I). The second paper of this study approaches the BCDs. To this end, we have acquired NIR deep images of 16 BCDs in the Virgo cluster. Using these data and our insights about dIs, we employ surface photometry to address the NIR morphology of BCDs in an attempt to provide new insight regarding possible evolutionary links between dIs and BCDs.

The organization of the present paper follows the one of Paper I. In §2 we present the sample selection criteria, and in §3 our observations. The image reduction method is presented in §4. Surface photometry will be addressed in §5. Photometric data are used in §6 to study the NIR properties of BCDs. Conclusions are presented in §7.

## 2. The Sample

The BCD candidates were selected according to the following criteria:

1. common distance, i.e. members of the Virgo Cluster as defined by the Virgo Cluster Catalog (VCC; Binggeli, Sandage and Tammann 1985; Binggeli, Tammann and Sandage 1987; Binggeli, Popescu and Tammann 1993);
2. classified as BCD or dI/BCD, according to the literature (i.e., NED);
3. availability of oxygen abundances, preferably from the [O III] $\lambda$ 4363 emission line;
4. low-density environment, as delineated by the X-ray map provided by the ROSAT All-Sky-Survey (Lee & Schindler 2001);
5. absolute magnitude between  $-12 \lesssim M_B \lesssim -16$ .

By restricting targets to the Virgo Cluster, we hoped to reduce scatter in distance-dependent parameters. By minimizing the density of intergalactic gas, we would avoid perturbations which might be caused by ram-pressure stripping (Lee, McCall and Richer 2003). Finally, by restricting the luminosity range, we hoped to be able to make a statistically relevant comparison with dIs. We identified 16 BCDs which satisfy these conditions. They are listed in Table 2.

In Paper I, it was shown that NIR surface brightness profiles of dIs flatten toward the centre. However, two nearby galaxies classified as dIs, namely NGC 1569 and NGC 3738, display centrally-peaked surface brightness profiles. NGC 1569, which has a distance modulus of  $DM = 26.37$  (Paper I), is well known for its central starburst activity (e.g., Greggio, et al. 1998; Aloisi, et al. 2001). NGC 3738, which is located in the Canes Venatici I cloud at  $DM = 29.27$ , also has been previously suggested to harbour stochastic star formation processes (Hunter, Gallagher and Rautenkranz 1990). Due to their NIR flux excesses at small radii, we add NGC 1569 and NGC 3738 to the Virgo BCD sample in this paper. We will show that their surface brightness profiles suggest that they are BCDs, not dIs.

### 3. Observations

Between 2001 and 2004 we had 4 observing runs (21 nights in total) on the 2.1 m telescope at the Observatorio Astronómico Nacional in the Sierra San Pedro Mártir (OAN-SPM) in Baja California, Mexico. The primary objective of the runs was to obtain deep imaging of a sample of Virgo BCDs in the NIR, all of which have known or soon-to-be-known metallicities.

All galaxies were observed in  $J$  and  $K_s$  bands using the CAMILA NIR camera at the  $f/13$  focus of the 2.1 m telescope. CAMILA is equipped with a NICMOS3  $256 \times 256$  pixel array (Cruz-Gonzales et al. 1994). The scale was  $0''.85 \text{ pix}^{-1}$ , yielding a field of view FOV  $3'.6 \times 3'.6$ .

The weather during Feb-Mar at OAN-SPM was unstable throughout the four runs, with clear skies less than half the allocated time and only one night with photometric conditions. Most of the allocated observing time was bright (Moon within 5 days of full), but this is less important when observing in the NIR, as moonlight brightens the sky by about 0.3 mag arcsec $^{-2}$  in  $K_s$  and about 0.9 mag arcsec $^{-2}$  in  $J^2$ .

---

<sup>2</sup>Cf. Vanzi & Hainaut (2002), online at European Southern Observatory, <http://www.eso.org/gen-fac/pubs/astclim/lasilla/l-vanzi-poster>

During the four runs, we imaged in  $J$  and  $K_s$  16 BCDs in Virgo. We took the data starting around local time 23h when the airmass was below  $\sim 1.8$ . Because of cirrus clouds most of the time, variable exposure times of 20–70 min in  $K_s$  and 15–40 min in  $J$  were used in order to reach  $\mu_{K_s} = 23 \text{ mag arcsec}^{-2}$  and  $\mu_J = 24 \text{ mag arcsec}^{-2}$ . These exposures were obtained by combining sequences of one-minute frames in both  $K_s$  and  $J$ . These one minute sub-exposures were acquired unguided. During the first run, we cycled the targets (VCC 24 and VCC 324 in  $K_s$ ) through the four quadrants of the chip. During the next three runs, we sampled the sky half as often as the targets in regions chosen randomly to be 4 to 5 arcmin away from the galaxies. Each galaxy frame was dithered by about  $3''$ . In short, we adopted the following observing sequence:

$$\text{sky} - \text{target} - \text{target} - \text{sky} - \text{target} - \text{target} - \text{sky} - \dots - \text{sky} - \text{target} - \text{target} - \text{sky} \quad (1)$$

We present the observing log for all four runs in Table 2. In the last column we include the full width at half maximum (FWHM), measured on a few stars in each reduced image.

We observed NGC 1569 and NGC 3738 on the Canada-France-Hawaii Telescope (CFHT) in Mar 2002, using exposures tuned to match the same surface brightness limit as our OAN-SPM Virgo observations. Details of the observations and data reduction of these two galaxies are given in Paper I.

#### 4. Data Reductions

One bad pixel map was built for each run using flat field images taken with two different exposure times. It was applied as the first step in the data reduction process to all our raw images (using the BADPIX task of IRAF).

For each filter, a flat field was built for each run from two series of twilight sky images taken with long and short exposure times. The low-signal flat was subtracted from the high-signal flat in order to produce the final flat field image.

Removal of the background represents the most important step in NIR observations, especially when observing the outer regions of faint galaxies (e.g., Vaduvescu & McCall 2004). In order to remove the variable airglow and thermal contributions, the sky frame observed close to each science frame was subtracted from the science frame. The sky-subtracted galaxy frames were divided by the flat field, then leveled additively by forcing the corners to zero. Finally, they were combined using the IMCOMBINE task in median mode, which eliminated the hot pixels, cosmic rays, and negative residuals that appear in the reduced frames after sky subtraction.

The collection of IRAF scripts created to reduce our data is available online<sup>3</sup>. The reduced  $J$ -band images of the 16 Virgo BCDs observed are presented in the left panel of Fig. 7.

Throughout our runs, we planned to observe Persson reference stars (Persson et al. 1998) to calibrate our observations. As only one night turned out to be photometric, we derived the zero-point for each reduced image using 3 to 12 2MASS stars appearing in each field. For most images, we estimate the zero-point errors to be less than 0.05 mag, with the maximum reaching about 0.2 mag in three sparsely populated cases: VCC 641 (including only one 2MASS star in the field), and VCC 144 and VCC 1313 (with only two 2MASS stars each).

## 5. Surface Photometry

Due to the relatively small telescope aperture and poor spatial resolution, it was not possible to resolve stars at the distance of Virgo. We employed the task ELLIPSE of the STSDAS package under IRAF to perform surface photometry.  $K_s$  observations were more affected than  $J$  by the poor weather conditions (high humidity and cirrus), so we preferred to use images in  $J$  to determine the ellipse fitting parameters.

We used the ELLIPSE task in two stages. First, we approximated the initial ellipse centres, ellipticities and position angles, but allowed them to vary freely with radius during the fitting. Then we plotted the fits using ISOPALL to analyze the outer isophotes where the underlying diffuse component is expected to reflect the geometry of the galaxy. At large radii (e.g., close to the semimajor axis given by NED<sup>4</sup>), the fitting parameters can be regarded as constant, none of them showing isophotal twists or tidal distortions in the outer regions. Using these values, in the second stage we fixed the centre, ellipticity, and the position angle and repeated the fitting process for both bandpasses. Setting the fitting parameters to be constant is a more robust approach to model a galaxy’s brightness in its outer regions. In Table 1, we include the measured eccentricities and position angles of our targets.

In Fig. 7, the upper graphs in the right panel beside each galaxy present surface brightness profiles in  $K_s$  and  $J$  for the BCDs observed at OAN-SPM. The profiles of NGC 1569 and NGC 3738 are included in the last two panels. The formal uncertainties in the surface

---

<sup>3</sup>The REDNIR.CL NIR image reduction scripts available at <http://www.geocities.com/ovidiv/astrsoft.html>

<sup>4</sup>NASA/IPAC Extragalactic Database (NED) is operated by the JPL, CALTECH, under contract with NASA

photometry as given by ELLIPSE are plotted as error bars. Most of the errors are less than  $0.1 \text{ mag arcsec}^{-2}$ . Ellipticity errors listed by ELLIPSE are less than 0.05 in most cases, and position angles are uncertain by about 2 degrees. For the faintest or the most compact targets (VCC 428, VCC 1313), we estimate that errors reach 0.1 in ellipticity and 5-10 degrees in position angle.

### 5.1. Isophotal Magnitudes

Using the ISOPLOT task of STSDAS, we have measured the *isophotal magnitude* ( $m_I$ ) of each BCD from the total flux integrated out to the faintest visible isophote, i.e., about  $\mu_{K_s} = 23 \text{ mag arcsec}^{-2}$  or  $\mu_J = 24 \text{ mag arcsec}^{-2}$ . We include the isophotal magnitudes in Table 4. The errors in the isophotal magnitudes are determined mainly by the zero points, whose typical uncertainties are less than 0.1 mag (see §4).

The 2MASS<sup>5</sup> extended source catalog includes 8 BCDs in common with our sample. Also, Goldmine<sup>6</sup> (Gavazzi, et al. 2003) lists NIR data for 9 BCDs observed by us. In Table 3 we compare the total magnitudes from these sources with our own. In most cases, both 2MASS and GOLDMine fluxes are below our fluxes, likely due to our fainter detection. The difference is larger for 2MASS, as much as 1 mag for VCC 848 (for which GOLDMine  $K_s$  data is much closer to our result).

### 5.2. Profile Decomposition

The exponential law,

$$I = I_0 \exp(-r/r_0) \quad (2)$$

and the de Vaucouleurs law,

$$I = I_e \exp \left( -7.67 \left( (r/r_e)^{\frac{1}{4}} - 1 \right) \right) \quad (3)$$

have been used extensively to model the surface brightness profiles (SBPs) of BCDs both in the visible and in the NIR. Here,  $I$  stands for the brightness at a given semimajor axis  $r$ ,  $I_0$  for the central surface brightness,  $I_e$  for the surface brightness at the effective radius, while  $r_0$  represents the exponential and  $r_e$  the effective radius within which half of the galaxy's total luminosity is contained.

---

<sup>5</sup>2MASS GATOR Catalog <http://irsa.ipac.caltech.edu/applications/Gator>

<sup>6</sup>GOLDMine - Galaxy Online Database Milano Network <http://goldmine.min.infn.it>



James (1994) fitted an exponential in order to model the luminosity profiles of five Virgo BCDs observed in the NIR, deriving exponential scale lengths and extrapolated central surface brightnesses. Analysing a sample of 44 BCDs observed in the visible, Doublier et al. (1997) and Doublier, Caulet, & Comte (1999) found that 25% of the SBPs fit a pure exponential profile, 18% have a dominating exponential component, 20% follow a pure de Vaucouleurs profile, 27% present a dominant de Vaucouleurs distribution, and the remaining 7% are unclassifiable. Using a subsample of 12 BCDs observed in the near-infrared, Doublier, Caulet, & Comte (2001) conclude that the NIR light distributions are generally consistent with those in the optical, although in some peculiar cases the brightness profiles differ significantly.

A combination of two or three different models has been employed by some authors to improve the fits to the surface brightness profiles. Gavazzi, et al. (2000) used the exponential law, the de Vaucouleurs law, or a combination of the two in order to fit the light profiles of dIs and BCDs observed in  $H$  and  $K_s$  in five nearby clusters. Using observations in the visible of 12 BCDs and 2 other bright starburst galaxies, Papaderos et al. (1996) decomposed profiles into three components: an exponential at large radii, a plateau at intermediate radii, and a Gaussian at small radii, with the last two supposedly describing the current starburst superimposed on the older stellar component.

Cairos et al. (2001) performed deep broadband observations in the visible on a sample of 28 BCDs. Over 70% of the galaxies showed complex profiles that precluded fitting with a single standard law (exponential or de Vaucouleurs), with extra structure at high to intermediate intensity levels. Using a subsample of 9 BCDs, Cairos et al. (2003) performed NIR surface photometry, finding that the morphology is basically the same as in the visible, with the inner regions dominated by the starburst component. Fits of Sersic laws were very sensitive to the selected radial interval. Fitting an exponential model gave more stable results.

Noeske et al. (2003) and Noeske et al. (2004) took deep NIR ( $J$ ,  $H$  and  $K_s$ ) images of a sample of 23 field BCDs with the Calar Alto 3.6m telescope in the North and the ESO 3.6m NTT in the South. To perform the surface photometry, the authors employed a complicated method (Papaderos et al. 2002) which uses isophotal masks defining “polygonal apertures” which follow the flux. This method is sensitive to the sky noise at large radii, to the imperfect manual cleaning of the field stars, and also to the starburst region at small radii where most of the SBPs are seen to brighten abruptly. Nevertheless, exponential fitting was found to approximate well the intensity distribution at large radii. The surface brightness profiles of some BCDs show a central flattening, the so-called “type V” profile, following the nomenclature of Binggeli & Cameron (1991). To describe this distribution, the authors

employed the “modified exponential distribution” - the *med* law (Papaderos et al. 1996a) - a complicated function involving two more constants,  $b$  and  $q$ , additional to the central intensity,  $I_0$ , and the exponential scale length,  $\alpha$ . However, a Sersic law was found to model the flattening at small radii, too, although a pure or modified exponential formula may be preferred to fit the underlying low surface brightness component of BCDs.

As mentioned previously, we derived our surface brightness profiles by fixing the ellipse parameters. Tying the profiles to the geometry of the smooth extended component instead of the light affected by the outburst region is a more robust approach to studying what underlies BCDs. We present our profiles in the right panels of Fig. 7. Most galaxies show an exponential profile in the outer regions, extending as low in surface brightness as  $\mu_{K_s} = 23 \text{ mag arcsec}^{-2}$  and  $\mu_J = 24 \text{ mag arcsec}^{-2}$ . At small radii, superposed on top of the exponential, most profiles show some excess over an exponential due to the starburst. Profiles often appear to level off at radii very close to zero. These trends have been found previously in dIs, suggesting some structural links with probable evolutionary implications for the two types of dwarfs (Papaderos et al. 1996).

As shown in Paper I, the NIR surface brightness profiles of dIs can be modeled using the following hyperbolic secant (*sech*) law:

$$I_S = I_{0S} \text{sech}(r/r_{0S}) = \frac{I_{0S}}{\cosh(r/r_{0S})} = \frac{2I_{0S}}{e^{r/r_{0S}} + e^{-r/r_{0S}}} \quad (4)$$

Here  $I_S$  represents the fitted *sech* flux at radius  $r$ , the distance from the centre along the semimajor axis.  $I_{0S}$  is the *sech central surface brightness* ( $m_{0S}$  in magnitude units), and  $r_{0S}$  represents the *sech scale length*.

We attempted to fit the profiles of BCDs using Equation 4 in combination with the following Gaussian component to model the starburst:

$$I_G = I_{0G} \exp \left( -\frac{1}{2} \left( \frac{r}{r_{0G}} \right)^2 \right) \quad (5)$$

Here  $I_G$  represents the fitted Gaussian flux at radius  $r$ , while  $I_{0G}$  is the *Gaussian central surface brightness* ( $m_{0G}$  in magnitude units), and  $r_{0G}$  represents the *Gaussian scale length*. The total fitted flux at radius  $r$  can be expressed as the sum of the two components:

$$I_T = I_S + I_G \quad (6)$$

Integrated over all radii, Equation 4 defines the *sech magnitude*,  $m_S$ , which we interpret as representative of the diffuse underlying component. Toward the centre, the *sech* profile

flattens and levels out at the *sech central surface brightness*,  $\mu_{0S}$ . The integral of Equation 5 determines the magnitude of the outburst,  $m_G$ .

To perform the fitting of the profiles generated by ELLIPSE, we employed the task NFIT1D (in the FITTING package of STSDAS), entering Equation (6) as our user specified function for the USERPAR/FUNCTION parameter. Fitted surface brightnesses were converted into magnitude units ( $\text{mag arcsec}^{-2}$ ) using the zero-points for the frames.

The fits to our surface brightness profiles in  $J$  and  $K_s$  are shown on the upper graphs in the right panels of Fig. 7. NGC 1569 and NGC 3738 are included in the last two panels. For  $K_s$  only, the two components are plotted individually as well, with a dashed line for the sech component and with a dotted line for the Gaussian. The fits (solid lines passing through the points) match the profiles very accurately from the core to the farthest regions. The sech component matches the total at large radii (where the solid and the dashed lines superpose), while the Gaussian burst contributes mostly in the cores. Note that the peak surface brightness of the Gaussian is as high as that of the underlying sech in most cases. Fits to NGC 1569 and NGC 3738 are much improved over those with a pure sech function (Paper I). Adopted solutions for parameters are summarized in Tables 4 and 5.

Due to the poor resolution and seeing, most of the Gaussian scale lengths are comparable with the seeing (columns  $r_{0G}$  from Tables 2 and  $FWHM$  from 4, respectively). In these cases, the Gaussian scale lengths have to be regarded with caution. For a few compact galaxies, sech fitting was biased by a central spike in surface brightness, heading to an overestimate of the total flux. In these cases, to prevent an inaccurate fit of the exponential at large radii and to account for the seeing (2 to 3'', cf. with Table 2), we restricted the fit to regions beyond about 3'' from the centre. Such intervals are marked by horizontal lines in our plots in Fig. 7. In only one case (VCC 848), we used different inner limits for the two bands; both limits are shown, corresponding to  $K_s$  (top) and  $J$  (bottom).

There are six galaxies which either were observed in poor weather conditions, have very small sizes (and, thus, poor sampling), or have unsure BCD classification. Some of these have profiles resembling those of dIs, which can be well fitted using the sech law alone (Paper I). Four BCDs give negative Gaussian central surface brightnesses, impossible physically. We re-fitted the surface brightness profiles of these six galaxies using a sech component alone. In Table 6, we compare the sech model (denoted by  $S$  in Column 3) with the two-component model (sech+Gaussian, denoted by  $S + G$ ).

Images in  $K_s$  for the following targets were especially affected by the poor weather conditions: VCC 428, VCC 1313, VCC 2033, and VCC 848. The first three are also compact, so profiles are poorly sampled. As a result of the loss of sensitivity, two consequences are

likely. First, we likely have less extent to fit the sech component due to the loss of the fainter isophotes. Second, combined with our low spatial resolution, sharp features may be blurred somewhat, resulting in Gaussian parameters that may be less reliable.

VCC 428 is a very compact galaxy observed under very poor conditions. A pure sech model matches  $m_T$  better and its rms errors are slightly smaller than those for the two-component model. Thus, we adopt the sech fit.  $K_s$  images for VCC 848 also were observed under poor conditions, although the rms errors in the two-component fit suggest a better fit than in the sech case. VCC 1313 is a very compact BCD, so it is not well sampled. The two-component model provides a smaller rms than the sech alone, so we adopt it. However, given the galaxy’s compact size and a surface brightness profile that is shallower than desirable, it is likely that the sech parameters of this composite fit are poorly determined and more uncertain than the formal errors indicate.

For VCC 1374 and VCC 1725, the fitting derives a negative Gaussian central surface brightness ( $\mu_{0G}$  marked as “n/a” in Table 6). According to NED, these two galaxies have ambiguous BCD classification, VCC 1374 being listed as “BCD?, IBm: sp”, VCC 1725 as “SmIII/BCD”. For both galaxies, a pure sech model produces better fits (chi-square and rms values are smaller), so we adopt it. VCC 1699 has a surface brightness profile resembling that of a dI, but its NED classification lists it as “SBmIII”, although it is listed as a BCD by De Paz, Madore and Pevunova (2003) and has been included as a dwarf HII galaxy by Vilchez and Iglesias-Paramo (2003). Its pure sech model provides a better match between the  $J$  and  $K_s$  scale radii, so we prefer to adopt this fit instead of the two-component one. In Fig. 7 we show the fit of the pure sech model for VCC 428, VCC 1374, VCC 1699, and VCC 1725, and the fit for the two component model for VCC 848 and VCC 1313.

The structural parameters for at least two galaxies, NGC 3738 and VCC 848, appear to be unusual. The radius of their Gaussian component in both  $K_s$  and  $J$  is at least a factor of two larger than that found for all the others. It is therefore not clear whether their Gaussian components represent the same phenomenon as in the other galaxies and may explain their sometimes anomalous positions in some of the diagrams that follow.

Included in Tables 4 and 5 are the sech central surface brightness,  $\mu_{0S}$ , the Gaussian central surface brightness,  $\mu_{0G}$ , in mag arcsec<sup>-2</sup>, the sech scale length,  $r_{0S}$ , and the Gaussian scale length,  $r_{0G}$ , in arcsec, for both  $J$  and  $K_s$ . Based upon the NFIT1D error analysis, the uncertainties in  $\mu_{0S}$  and  $\mu_{0G}$  are less than  $\sim 0.1$  mag arcsec<sup>-2</sup>. The sech scale lengths in the two bands agree to within about 0.5 arcsec (about 5%) for most galaxies, but the Gaussian scale lengths show larger differences, possibly due to variations in image quality.

### 5.3. Sech and Gaussian Magnitudes

The integrated magnitude of the sech component of a BCD can be calculated from Equation (4) by integrating the surface brightness over radii from zero to infinity (Paper I):

$$m_S = zp_s - 2.5 \log (11.51 I_{0S} r_{0S}^2 (1 - e)) \quad (7)$$

Here  $I_{0S}$  is the sech central surface brightness,  $r_{0S}$  is the sech scale length,  $e$  represents the galaxy ellipticity, and  $zp_s$  is the frame zero-point.

The flux due to the starburst can be quantified similarly by integrating Equation (5). Let  $a$  and  $b$  be the semimajor and semiminor axis of the isophotes, and  $I_G(a)$  the average surface brightness of the Gaussian component in an elliptical annulus with area  $dA$ :

$$dA = d(\pi ab) = d(\pi a^2(1 - e)) = 2\pi a(1 - e)da \quad (8)$$

Then, the total flux  $I_G$  due to the Gaussian component is given by:

$$I_G = \int_0^\infty I_G(a) dA = 2\pi(1 - e) I_{0G} \int_0^\infty a \exp(-0.5(a/r_{0G})^2) da \quad (9)$$

By substituting  $x = a/r_{0G}$  in the last integral, the integrated Gaussian flux becomes:

$$I_G = 2\pi(1 - e) I_{0G} r_{0G}^2 \int_0^\infty x \exp\left(\frac{-x^2}{2}\right) dx = 2\pi(1 - e) I_{0G} r_{0G}^2 \quad (10)$$

With this result, the *Gaussian magnitude* can be calculated from:

$$m_G = zp_s - 2.5 \log I_G \quad (11)$$

Included in Table 4 for each galaxy are the *sech magnitude* ( $m_S$ ), the *Gaussian magnitude* ( $m_G$ ), and the *total magnitude* ( $m_T$ ) computed from the sum of the sech and the Gaussian fluxes. Formal uncertainties in  $m_S$  and  $m_G$  are typically  $\sim 0.1$  mag. As one can see, total magnitudes are very close to the isophotal magnitudes (in most cases within 0.05 mag). This is visualized in Fig. 2, which plots the difference between the total magnitude and the isophotal magnitude versus the isophotal magnitude in  $K_s$ . A few outliers are labelled, all of which were observed under particularly difficult circumstances.

In Fig. 3 we plot the difference between  $m_S$  and  $m_I$  as a function of isophotal magnitude. In  $K_s$ , sech magnitudes are within about 0.4 mag of the isophotal magnitudes, showing that the flux from the starburst is small relative to the total NIR flux. Sudarsky & Salzer 1995 and Salzer & Norton 1999 estimated that the starburst in the visible enhances the flux by 0.6 – 1.0 mag and 0.75 mag, respectively, on average. Thus, the relative visibility of the underlying component is improved in the NIR.

#### 5.4. Isophotal Radii

Using Equation (4), we have calculated the semimajor axis  $r_{22}$  corresponding to  $K_s = 22$  mag arcsec<sup>-2</sup> as well as  $r_{23}$  corresponding to  $J = 23$  mag arcsec<sup>-2</sup>. The positive solution for the 2nd order equation in  $r_{22}$  comes to

$$r_{22} = r_{0S} \ln \frac{1 + \sqrt{1 - A_{22}^2}}{A_{22}} \quad (12)$$

where  $A_{22}$  is given by:

$$\log A_{22} = \frac{zp_s - 22 - 2.5 \log I_{0S}}{2.5} \quad (13)$$

There is a similar formula for  $r_{23}$ . Our values for  $r_{22}$  and  $r_{23}$  are listed in Table 4. Based upon the NFIT1D error analysis, we evaluate typical uncertainties in  $r_0$ ,  $r_{22}$  and  $r_{23}$  to be about 2%.

#### 5.5. Color Profiles

Color profiles were derived by subtracting  $J$  and  $K_s$  surface brightnesses via the TCALC task of TABLES (STSDAS package). For each galaxy, the color profile is given in Fig. 7 below the surface brightness profile (to the right of the galaxy image). Most galaxies show a remarkably constant  $J - K_s = 0.7$  to  $0.9$  mag. Bursts appear to have little effect on NIR colors.

### 6. NIR Properties of BCDs

#### 6.1. Correlations

Below, we examine correlations among the different parameters of BCDs included in Table 4. For sizes, we employ the semimajor axes,  $r_{22}$  for  $K_s$ , and  $r_{23}$  for  $J$ . To trace the diffuse component, we use the absolute sech magnitudes  $M_S$ , while for the total light we use the absolute isophotal and total magnitudes  $M_I$  and  $M_T$ , respectively. We trace the strength of the starburst with the absolute Gaussian magnitude,  $M_G$ . To characterize the structure of the diffuse cores, we employ the sech central surface brightness  $\mu_{0S}$  and the sech scale length  $r_{0S}$ , expressed in kpc. We focus on the  $K_s$  band because of its reduced sensitivity to the light of hot stars, but similar results are obtained in  $J$ . To compare properties of BCDs with dIs, we overlay on some plots our field dI data from Paper I. In each graph to be discussed,

typical uncertainties in each parameter are plotted as an error cross. For the Virgo galaxies, absolute magnitudes and scale lengths are calculated assuming a common distance modulus,  $DM=30.62$  (Freedman et al. 2001), which is the HST Key Project distance to the Virgo Cluster anchored to the maser distance for NGC 4258 (Paper I).

### 6.1.1. Size and Brightness

In the visible ( $B$  band), emission-line galaxies (mostly BCDs) and gas rich dwarfs display a linear relationship between the log of the disk scale length and the absolute magnitude (Vennik, Hopp and Popescu 2000; Bergvall et al. 1999). A similar trend has been found in the NIR for dwarf galaxies, including BCDs (Papaderos et al. 1996, 2002). The correlation for the BCDs appears to be steeper than the correlation for other dwarfs, in the sense that, for a given  $B$  luminosity, BCDs have smaller scale lengths by a factor of  $\sim 2$  than other dwarf galaxies (Papaderos et al. 1996). A similar trend was found by Boselli et al. (1997) between the NIR concentration index  $c_{31}$  (defined as the ratio between the radii that contain 75% and 25% of light) and the magnitude (see their Fig. 10) for late-type galaxies in Virgo.

In Fig. 4, we plot the sech scale length  $r_{0S}$  versus the sech absolute magnitude  $M_S$  for our BCD sample (filled symbols). dIs from Paper I are shown as open symbols, and the linear fit to the dIs from Paper I is shown as a dotted line. The star burst dIs NGC 1569 and NGC 3738 are labeled. VCC 848 is an outlier, whose data was acquired under poor weather conditions. VCC 1699, VCC 1725 and VCC 1374 were fitted using the sech component alone. For the brighter BCDs, scale length does appear systematically smaller compared to dIs at a given absolute magnitude.

Using two BCD samples observed in the visible (22 and 23 targets) and a subsample observed in the NIR (11 targets), Doublier et al. (1997) and Doublier, Caulet, & Comte (1999, 2001) found a linear trend between the log of the effective radius and the absolute magnitude, in the sense that brighter galaxies have larger sizes. A similar relation was found by Vennik, Hopp and Popescu (2000) in the visible for a larger sample which included about 115 BCDs. Fig. 5 plots the semimajor axis  $r_{22}$  versus the absolute isophotal magnitude  $M_I$  in  $K_s$ . BCDs are marked with filled symbols and dIs with open circles. The fit to the dIs derived in Paper I is shown as a dashed line. As in Fig. 4, VCC 848 and VCC 1699 are outliers. The BCDs display a trend similar to that of dIs, albeit with more scatter. The enhanced scatter is greater than can be explained by the inclusion of the starburst in  $M_I$ .

### 6.1.2. Central Surface Brightness

Vennik, Hopp and Popescu (2000) did not find any correlation between the extrapolated central surface brightness of an exponential and the absolute  $B$  magnitude for a large sample of emission-line galaxies (mostly BCDs) observed in the visible. However, using another large sample of dwarf galaxies including BCDs, dIs and dEs, Papaderos et al. (1996) and Papaderos et al. (2002) found a trend between the central surface brightness of the exponential and the total  $B$  magnitude, although the correlation was very loose.

In Fig. 6, we present the correlation between the sech central surface brightness  $\mu_{0S}$  and the absolute sech magnitude  $M_{S,K}$  in  $K_s$ . BCDs and the two starburst dIs are plotted with filled symbols and dIs from Paper I are plotted with open symbols. BCDs and dIs follow similar trends, although luminous BCDs might have systematically brighter central surface brightnesses than luminous dIs. The two star burst field dIs are labeled. VCC 848 is an outlier observed in poor weather, while VCC 1725 and VCC 1699 were fitted using sech component alone. Using 38 dIs and BCDs in our two samples, the following relation is derived:

$$M_{S,K} = (1.52 \pm 0.08)\mu_{0S,K} - (46.51 \pm 1.35) \quad (14)$$

The fit is shown as a dotted line in Fig. 6. The rms deviation of points about the fit is 0.84 mag.

### 6.1.3. Starbursts

Fig. 7 plots the Gaussian magnitude  $M_G$  versus the sech magnitude  $M_S$  for our BCD sample. Objects with brighter underlying components seem to have larger bursts. VCC 1313's position may well be the result of the poorer quality of the data available for it. Fig. 8 shows the strength of the burst relative to the diffuse component ( $M_G - M_S$ ) versus  $M_S$ . There is no obvious correlation, which indicates that burst strength scales linearly with mass. In other words, there is no evidence for triggering of star formation in more massive hosts over and above what is expected for a large reservoir of matter. VCC 1313's position may well be the result of the poorer quality of the data available to it.

### 6.1.4. Fundamental Plane

For spiral galaxies, absolute magnitudes are tightly correlated with the log of the HI line-width  $W_{20}$  after correcting for projection (Tully & Fisher 1977). However, the correlation



is poor for late-type galaxies, even when NIR data is employed (Pierini & Tuffs 1999, Paper I). In Paper I it was discovered that residuals in the Tully-Fisher relation for dIs were linked to the central surface brightness of the sech profile,  $\mu_{0S}$ . A “fundamental plane” was defined for the dIs, relating  $M_S$  to  $\mu_{0S}$  and  $\log W_{20}$ . In Fig. 9, we reproduce this fundamental plane, representing dIs from Paper I as empty symbols and the BCDs as filled symbols. Although BCDs show more scatter than the dIs, they are concentrated around the plane, suggesting that BCDs are dynamically similar to dIs. The two star burst field dIs, NGC 1569 and NGC 3738, are labeled, along with the most outlier Virgo BCDs. The larger scatter of BCDs about the plane is mainly due to the large uncertainties in  $W_{20}$ , as high as 13 km/s, which translates into 4.5 mag in the first term of the X axis. Also it could be due to intrinsic factors affecting the line widths, such as turbulence or winds and to differences in distances due to the cluster depth.

## 7. Conclusions

Blue compact dwarfs (BCDs) and dwarf irregulars (dIs) are important probes for studying the formation and evolution of galaxies. In an effort to extract information about old stellar populations, a sample of 16 BCDs in the Virgo Cluster have been imaged using a NIR array at the OAN-SPM in Mexico.

Surface brightness profiles were successfully modeled using only two functions (four free parameters): a hyperbolic secant (sech) tracing the diffuse component (responsible for most of the light), and a Gaussian for the central starburst. A hyperbolic secant is known to fit the near-IR profiles of dIs. Isophotal, sech, and total (sech plus Gaussian) NIR magnitudes were calculated for all galaxies. Also, semimajor axes at  $\mu_J = 23 \text{ mag arcsec}^{-2}$  and  $\mu_{K_s} = 22 \text{ mag arcsec}^{-2}$  were determined from the sech fit.

We searched for relations between semimajor axes, scale length, absolute magnitude (sech, isophotal, total, and Gaussian), central surface brightness, and color. Correlations between the sech scale length and the sech magnitude, sech surface brightness and sech magnitude, and between the sech semimajor axis and the total magnitude overlap those of dIs, though with more scatter. Overall, BCDs with more luminous diffuse components are larger and have brighter cores, as is also found for dIs. The central burst appears to correlate with the luminosity of the diffuse component, with brighter BCDs having stronger star bursts. However, the strength of the burst relative to the diffuse component shows no trend with luminosity, indicating that more luminous bursts are simply a consequence of a larger reservoir of matter, not extra triggering. Color profiles show a relatively constant  $J - K_s = 0.7$  to  $0.9 \text{ mag}$  at all radii. The diffuse component represents the overwhelming

majority of the NIR light for most BCDs, the starburst enhancing the flux by less than about 0.3 mag.

BCDs lie on the fundamental plane of dIs (Paper I), showing the same relation between the sech absolute magnitude, the sech central surface brightness, and the hydrogen line-width. However, the scatter about this plane is larger than for the dIs, perhaps due to enhanced turbulence or winds. It is concluded that BCDs and dIs are similar structurally and dynamically.

We thank the OAN-SPM time allocation committees for granting us the opportunity to observe. MGR acknowledges financial support from CONACyT grant 37214-E and DGAPA-UNAM grant IN114199. Special thanks to F. Montalvo, S. Monrroy, and G. Melgoza, for their help with the observations. MLM thanks the Natural Sciences and Engineering Council of Canada for its continuing support. For our data reductions, we used IRAF, distributed by the National Optical Astronomy Observatories, which are operated by the Association of Universities for Research in Astronomy, Inc., under cooperative agreement with the National Science Foundation. This research has made use of the GOLDMine Database in Milano and the NASA/IPAC Extragalactic Database (NED) which is operated by the JPL, CALTECH, under contract with NASA.

## REFERENCES

- Aloisi, A., et al., 2001, *AJ*, 121, 1425
- Arp, H., 1965, *ApJ*, 142, 383
- Bergvall, N., et al., 1999, *A&A*, 341, 697
- Binggeli, B., and Cameron, L. M., 1991, *A&A*, 252, 27
- Binggeli, B., Popescu, C. C., Tammann, G. A., 1993, *A&A*, 98, 275
- Binggeli, B., Sandage, A., Tammann, G. A., 1985, *AJ*, 90, 1681
- Binggeli, B., Tammann, G. A., Sandage, A., 1987, *AJ*, 94, 251
- Bosseli, A., et al., 1997, *A&A*, 121, 507
- Cairos, L. M., et al., 2001, *ApJS*, 133, 321
- Cairos, L. M., et al., 2003, *ApJ*, 593, 312

- Cruz-Gonzales, I., et al., 1994, in *Instrumentation in Astronomy VIII*, D. L. Crawford and E. R. Craine, editors, SPIE, 2198, 774-780
- De Paz, A. G., Madore, B. F., Pevunova, O., 2003, *ApJS*, 147, 29
- Doublier, V., et al. 1997, *A&AS*, 124, 405
- Doublier, V., Caulet, A., & Comte, G. 1999, *A&AS*, 138, 213
- Doublier, V., Caulet, A., & Comte, G. 2001, *A&A*, 367, 33
- Fanneli, M. N., O’Connell, R. W., and Thuan, T. X., 1988, *ApJ*, 334, 665
- Freedman, W. L., et al. 2001, *ApJ*, 553, 47
- Gavazzi G., et al., 2000, *A&A*, 361, 863
- Gavazzi G., et al., 2003, *A&A*, 400, 451
- Greggio, L., et al., 1998, *AJ*, 504, 725
- Hidalgo-Gamez, A. M., and Olofsson, K., 1998, *A&A*, 334, 45
- Hunter, D. A., Gallagher, J. S., and Rautenkranz, D., 1990, *BAAS*, 12, 838H
- Izotov, Y. I., and Thuan, T. X., 1999, *ApJ*, 511, 639
- James, P. A., 1994, *MNRAS*, 269, 176
- Kunth, D., and Ostlin, G., 2000, *A&A Review*, Vol. 10, Issue 1/2, pp. 1-79
- Lee, H., and Schindler, S., 2001, private communication
- Lee, H., McCall, M. L. and Richer, M. G., 1993, *AJ*, 125, 2975
- Noeske, K. G., et al., 2003, *A&A*, 410, 481
- Noeske, K. G., et al., 2004, astro-ph/0409741 (accepted in *A&A*)
- Papaderos, P, et al., 1996a, *A&AS*, 120, 207
- Papaderos, P, et al., 1996, *A&A*, 314, 59
- Papaderos, P, et al., 2002, *A&A*, 393, 461
- Persson, S. E., et al., 1998, *AJ*, 116, 2475

- Pierini, D., & Tuffs, R. J. 1999, A&A, 343, 751
- Salzer, J. J., & Norton, S. A., 1999, ASP Conf. Series, 170, 253
- Scodeggio, M., et al., 2002, A&A, 384, 812
- Searle, L., & Sargent, W. L. W., 1972, ApJ, 173, 25
- Sudarsky, D. L., & Salzer, J. J., 1995, AAS Meeting 186, BAAS, 27, 867
- Thuan, T. X., & Martin, G. E., 1981, ApJ, 247, 823
- Thuan, T. X., 1983, ApJ, 268, 667
- Thuan, T. X., 1985, ApJ, 299, 881
- Tully, R. B., and Fisher, J. R. 1977, A&A, 54, 661
- Vaduvescu, O., & McCall, M. 2004, PASP, 116, 820
- Vaduvescu, O., et al, 2005 (Paper I), AJ, submitted
- Vaduvescu, O., PhD, 2005, *Infrared Properties of Star Forming Dwarf Galaxies*, PhD Thesis, York University.
- Vennik, J., Hopp, U., and Popescu, C. C., 2000, A&A, 142, 399
- Vilchez, J. M., & Iglesias-Paramo, J., 2003, ApJS, 145, 225
- Zwicky, F., 1965, ApJ, 142, 1293
- Zwicky, F., 1970, Advances in Astronomy and Astrophysics, Vol. 7 (New York: Academic Press)
- Zwicky, F., & Zwicky, M. A., 1971, Catalogue of Selected Compact Galaxies and of Post-Eruptive Galaxies (Zurich: Offsetdruck, L. Speich)

Table 1. Galaxy Sample

Galaxy (1)	$\alpha$ (J2000) (2)	$\delta$ (J2000) (3)	$e$ (4)	$PA$ (5)
VCC 24	12:10:35.6	+11:45:39	0.35	–25
VCC 144	12:15:18.3	+05:45:39	0.30	–65
VCC 213	12:16:56.0	+13:37:31	0.15	–70
VCC 324	12:19:09.9	+03:51:21	0.25	+30
VCC 334	12:19:14.2	+13:52:56	0.00	0
VCC 428	12:20:40.2	+13:53:20	0.60	+40
VCC 459	12:21:11.3	+17:38:19	0.40	+60
VCC 641	12:23:28.4	+05:48:59	0.40	–60
VCC 802	12:25:28.7	+13:29:50	0.65	+57
VCC 848	12:25:52.5	+05:48:36	0.65	+35
VCC 1313	12:30:48.5	+12:02:42	0.40	+73
VCC 1374	12:31:38.0	+14:51:24	0.60	–18
VCC 1437	12:32:33.5	+09:10:25	0.26	+75
VCC 1699	12:37:03.0	+06:55:36	0.50	+55
VCC 1725	12:37:41.2	+08:33:33	0.40	–65
VCC 2033	12:46:04.4	+08:28:35	0.10	+40

Note. — Col. (1): Galaxy name; Col. (2): Right ascension (listed by NED); Col. (3): Declination (listed by NED); Col. (4): Ellipticity ( $1-b/a$ ), from this paper; Col. (5): Position angle of major axis (North through East), from this paper;

Table 2. Observing Log

Galaxy	Date (UT)	Filter	Exp Time (sec)	FWHM (arcsec)
VCC 24	2002 Feb 26	<i>J</i>	600	2.1
	2001 Mar 1	<i>K<sub>s</sub></i>	3720	2.5
VCC 144	2003 Mar 14	<i>J</i>	1200	2.0
	2003 Mar 19	<i>K<sub>s</sub></i>	2340	2.2
VCC 213	2003 Mar 19	<i>J</i>	1200	2.3
	2003 Mar 19	<i>K<sub>s</sub></i>	2160	2.5
VCC 324	2002 Feb 26	<i>J</i>	600	2.0
	2001 Mar 2	<i>K<sub>s</sub></i>	3660	2.5
VCC 334	2003 Mar 19	<i>J</i>	660	2.2
	2003 Mar 19	<i>K<sub>s</sub></i>	1320	2.8
VCC 428	2004 Feb 17	<i>J</i>	1200	2.3
	2004 Feb 17	<i>K<sub>s</sub></i>	2340	2.0
VCC 459	2004 Feb 12	<i>J</i>	1200	1.8
	2004 Feb 12	<i>K<sub>s</sub></i>	2400	2.4
VCC 641	2002 Feb 26	<i>J</i>	600	2.2
	2003 Mar 17	<i>K<sub>s</sub></i>	4500	2.6
VCC 802	2004 Feb 14,15	<i>J</i>	1800	2.6
	2004 Feb 14	<i>K<sub>s</sub></i>	2280	2.3
VCC 848	2004 Feb 12	<i>J</i>	2400	2.4
	2004 Feb 12	<i>K<sub>s</sub></i>	2340	2.3
VCC 1313	2004 Feb 15,16	<i>J</i>	2400	2.5
	2004 Feb 15,16,17	<i>K<sub>s</sub></i>	4560	3.0
VCC 1374	2004 Feb 13	<i>J</i>	1200	2.5
	2004 Feb 13	<i>K<sub>s</sub></i>	2160	2.5
VCC 1437	2003 Mar 14	<i>J</i>	1680	1.9
	2002 Feb 28	<i>K<sub>s</sub></i>	2700	2.4
VCC 1699	2004 Feb 14,17	<i>J</i>	2400	2.6
	2004 Feb 14,16	<i>K<sub>s</sub></i>	4440	2.4
VCC 1725	2004 Feb 13	<i>J</i>	1200	2.6
	2004 Feb 13	<i>K<sub>s</sub></i>	2340	2.6
VCC 2033	2003 Mar 14	<i>J</i>	1200	2.0
	2002 Feb 28	<i>K<sub>s</sub></i>	1200	1.8

Table 3. Comparison of Apparent Magnitudes

Galaxy (1)	$\Delta m_J$ (2)	$\Delta m_K$ (3)	Reference (4)
VCC 24	-0.02	-0.21	2MASS
		+0.04	GOLDMine
VCC 144	+0.09	+0.27	2MASS
VCC 213	+0.24	+0.13	2MASS
VCC 324	+0.25	+0.19	2MASS
	+0.00	-0.09	GOLDMine
VCC 334	-0.07	-0.39	GOLDMine
VCC 428			
VCC 459	+0.33	+0.04	2MASS
		+0.29	GOLDMine
VCC 641			
VCC 802		+0.56	GOLDMine
VCC 848	+1.06	+1.00	2MASS
		+0.34	GOLDMine
VCC 1313			
VCC 1374	+0.39	+0.44	2MASS
	-0.11	+0.06	GOLDMine
VCC 1437	+0.09	+0.10	2MASS
VCC 1699		+0.59	GOLDMine
VCC 1725	+0.40	+0.52	GOLDMine
VCC 2033	+0.27	+0.35	2MASS
		+0.58	GOLDMine

Note. — Col. (1): Galaxy name; Col. (2): Difference in  $J$  magnitude (reference minus this paper); Col. (3): Difference in  $K_s$  magnitude (reference minus this paper); Col. (4): Reference.

Table 4. Photometric Parameters

Galaxy	Filter	$m_I$ (mag)	$m_S$ (mag)	$m_G$ (mag)	$m_T$ (mag)	$\mu_{0S}$ (mag/sq."')	$r_{0S}$ (")	$\mu_{0G}$ (mag/sq."')	$r_{0G}$ (")	$r_{23(22)}$ (")
(1)	(2)	(3)	(4)	(5)	(6)	(7)	(8)	(9)	(10)	(11)
VCC 24	$J$	13.56	13.70	16.08	13.59	18.34	3.1	18.86	1.8	15.4
	$K_s$	12.78	13.09	14.58	12.84	17.65	3.0	17.73	2.1	14.0
VCC 144	$J$	13.46	13.85	14.95	13.51	18.39	2.8	17.88	1.8	14.1
	$K_s$	12.57	12.89	14.18	12.60	17.28	2.7	17.25	2.0	13.4
VCC 213	$J$	11.90	11.98	14.84	11.90	17.75	4.6	17.68	1.6	25.2
	$K_s$	11.12	11.21	14.07	11.14	16.94	4.5	16.85	1.6	23.9
VCC 324	$J$	12.53	12.52	15.85	12.47	19.54	8.6	19.69	2.7	33.4
	$K_s$	11.83	11.92	14.66	11.84	18.86	8.3	18.60	2.8	29.7
VCC 334	$J$	13.71	13.89	15.52	13.68	19.46	3.8	19.37	2.3	15.1
	$K_s$	13.13	13.25	15.25	13.09	18.77	3.7	18.85	2.1	13.7
VCC 428	$J$	15.88	15.82	(a)	15.82	21.05	5.2	(a)	(a)	12.9
	$K_s$	14.90	14.85	(a)	14.85	20.39	6.0	(a)	(a)	12.9
VCC 459	$J$	12.98	13.12	15.50	13.00	18.81	5.2	19.43	3.1	23.8
	$K_s$	12.31	12.46	14.81	12.34	18.10	5.1	18.76	3.2	21.8
VCC 641	$J$	14.36	14.53	16.28	14.33	19.90	4.5	20.26	3.2	16.0
	$K_s$	13.27	13.37	16.00	13.28	18.70	4.4	20.62	4.3	16.5
VCC 802	$J$	14.94	14.96	17.00	14.81	21.63	10.7	22.70	9.3	20.8
	$K_s$	14.25	14.23	18.55	14.21	20.57	9.2	20.35	1.5	18.4
VCC 848	$J$	13.39	13.55	15.06	13.31	20.80	14.0	20.16	7.1	38.1
	$K_s$	12.57	12.71	14.02	12.42	20.17	15.5	19.06	6.8	36.7
VCC 1313	$J$	15.82	16.59	16.55	15.82	20.91	2.8	19.89	2.4	7.2
	$K_s$	15.10	15.56	16.21	15.09	19.85	2.7	19.57	2.4	7.3
VCC 1374	$J$	13.34	13.32	(a)	13.32	19.88	9.5	(a)	(a)	34.0
	$K_s$	12.45	12.46	(a)	12.46	18.95	9.2	(a)	(a)	32.3
VCC 1437	$J$	12.84	13.14	14.53	12.87	18.28	3.7	17.21	1.6	18.4
	$K_s$	11.93	12.25	13.57	11.97	17.27	3.4	16.38	1.7	17.4
VCC 1699	$J$	12.49	12.50	(a)	12.50	19.86	12.3	(a)	(a)	44.2
	$K_s$	11.60	11.72	(a)	11.72	19.04	12.1	(a)	(a)	41.4
VCC 1725	$J$	12.73	12.81	(a)	12.81	20.12	11.0	(a)	(a)	36.9
	$K_s$	11.74	11.81	(a)	11.81	19.23	11.6	(a)	(a)	37.6
VCC 2033	$J$	13.41	13.59	15.74	13.45	19.23	4.1	19.48	2.3	17.3
	$K_s$	12.45	12.71	15.00	12.59	18.34	4.1	18.58	2.2	16.8

<sup>(a)</sup> Gaussian component not fitted

Note. — Col. (1): Galaxy name; Col. (2): Filter; Col. (3): Isophotal magnitude; Col. (4): Sech magnitude (from sech law); Col. (5): Gaussian magnitude (from Gaussian law); Col. (6): Total (Sech + Gaussian) magnitude; Col. (7): Central surface brightness of sech component; Col. (8): Scale length of sech component; Col. (9): Central surface brightness of Gaussian component; Col. (10): Scale length of Gaussian component; Col. (11): Semimajor axis  $r_{23}$  corresponding to the  $J = 23$  mag arcsec<sup>-2</sup>; semimajor axis  $r_{22}$  corresponding to  $K_s = 22$  mag arcsec<sup>-2</sup>.



Table 5. Local Volume dIs with BCD-like profiles

Galaxy	Filter	$m_I$ (mag)	$m_S$ (mag)	$m_G$ (mag)	$m_T$ (mag)	$\mu_{0S}$ (mag/sq.'')	$r_{0S}$ ('' )	$\mu_{0G}$ (mag/sq.'')	$r_{0G}$ ('' )	$r_{23(22)}$ ('' )
(1)	(2)	(3)	(4)	(5)	(6)	(7)	(8)	(9)	(10)	(11)
NGC 1569	$J$	9.06	9.38	10.67	9.09	17.99	21.0	17.14	10.6	111.3
	$K_s$	8.12	8.47	9.60	8.14	17.13	21.5	16.16	11.0	111.1
NGC 3738	$J$	10.46	10.67	11.97	10.39	19.67	22.2	19.40	14.6	63.9
	$K_s$	9.61	9.72	11.40	9.51	18.67	21.7	18.45	12.2	81.7

Note. — Col. (1): Galaxy name; Col. (2): Filter; Col. (3): Isophotal magnitude; Col. (4): Sech magnitude (from sech law); Col. (5): Gaussian magnitude (from Gaussian law); Col. (6): Total (Sech + Gaussian) magnitude; Col. (7): Central surface brightness of sech component; Col. (8): Scale length of sech component; Col. (9): Central surface brightness of Gaussian component; Col. (10): Scale length of Gaussian component; Col. (11): Semimajor axis  $r_{23}$  corresponding to the  $J = 23$  mag arcsec $^{-2}$ ; semimajor axis  $r_{22}$  corresponding to  $K_s = 22$  mag arcsec $^{-2}$ .

Table 6. Sech and Sech+Gaussian SBP fitting for six BCDs with dI-like profiles

Galaxy	Filter	Fit	rms	$m_I$	$m_T$	$\mu_{0S}$	$r_{0S}$	$\mu_{0G}$	$r_{0G}$	$r_{23(22)}$
(1)	(2)	(3)	(4)	(mag)	(mag)	(mag/sq."')	(")	(mag/sq."')	(")	(")
VCC 428	$J$	S	0.010	15.88	15.82	21.05	5.2	–	–	12.9
	$J$	S+G	0.013	15.88	15.76	21.90	6.8	21.69	4.9	11.4
	$K_s$	S	0.041	14.90	14.85	20.39	6.0	–	–	12.9
	$K_s$	S+G	0.044	14.90	14.77	20.49	6.5	20.47	0.9	13.3
VCC 848	$J$	S	0.037	13.39	13.61	19.69	8.2	–	–	23.1
	$J$	S+G	0.009	13.39	13.31	20.80	14.0	20.16	7.1	38.1
	$K_s$	S	0.055	12.57	12.82	18.76	7.7	–	–	28.3
	$K_s$	S+G	0.020	12.57	12.42	20.17	15.5	19.06	6.8	36.7
VCC 1313	$J$	S	0.017	15.82	15.80	19.43	2.0	–	–	6.2
	$J$	S+G	0.007	15.82	15.82	20.91	2.8	19.89	2.4	7.2
	$K_s$	S	0.028	15.10	15.10	18.82	2.1	–	–	7.6
	$K_s$	S+G	0.027	15.10	15.09	19.85	2.7	19.57	2.4	7.3
VCC 1374	$J$	S	0.033	13.34	13.32	19.88	9.5	–	–	34.0
	$J$	S+G	0.033	13.34	13.42	19.04	7.2	n/a	6.9	31.3
	$K_s$	S	0.043	12.45	12.46	18.95	9.2	–	–	32.3
	$K_s$	S+G	0.074	12.45	12.55	17.96	6.8	n/a	6.8	30.2
VCC 1699	$J$	S	0.017	12.49	12.50	19.86	12.3	–	–	44.2
	$J$	S+G	0.016	12.49	12.54	19.77	11.7	n/a	6.4	43.0
	$K_s$	S	0.036	11.60	11.72	19.04	12.1	–	–	41.4
	$K_s$	S+G	0.022	11.60	11.49	20.36	21.0	19.42	11.4	46.0
VCC 1725	$J$	S	0.025	12.73	12.81	20.12	11.0	–	–	36.9
	$J$	S+G	0.027	12.73	12.73	20.30	12.2	21.59	5.1	38.9
	$K_s$	S	0.039	11.74	11.81	19.23	11.6	–	–	37.6
	$K_s$	S+G	0.049	11.74	11.80	18.55	10.1	n/a	11.6	39.2

Note. — Col. (1): Galaxy name; Col. (2): Filter; Col. (3): Fit (S=sech; S+G=sech+Gaussian); Col. (4): rms error of fit; Col. (5): Isophotal magnitude; Col. (6): Total magnitude (sech or sech+Gaussian); Col. (7): Central surface brightness of sech component; Col. (8): Scale length of sech component; Col. (9): Central surface brightness of Gaussian component; Col. (10): Scale length of Gaussian component; Col. (11): Semimajor axis  $r_{23}$  corresponding to the  $J = 23$  mag arcsec $^{-2}$ , semimajor axis  $r_{22}$  corresponding to  $K_s = 22$  mag arcsec $^{-2}$ .

**Full version including figures available at**  
**<http://aries.phys.yorku.ca/~ovidiu/Paper3.ps.gz>**  
**( 5 MB gzip - sorry, too big for arXiv.org to store)**

Fig. 1.— Virgo BCD galaxies observed at OAN-SPM. Left panel:  $J$  images (North up, East to left, field  $3'0 \times 3'0$ ). Right panel: surface brightness profiles in  $J$  and  $K_s$  (upper graphs), and  $J - K_s$  color profiles (lower graphs). To make them more visible, the surface brightness profiles in  $J$  have been shifted by one magnitude. Solid lines passing through the points represent total (sech plus Gaussian) fits. For  $K_s$  only, sech and Gaussian components are plotted individually as well, with a dashed line and a dotted line, respectively. For VCC 428, VCC 1374, VCC 1699 and VCC 1725, the sech component is plotted as a solid line, because that was the only component fitted. Error bars are those calculated by ISOPLOT. NGC 1569 and NGC 3738, star burst dIs with BCD-like profiles observed at CFHT (Paper I) are included in the last two panels.

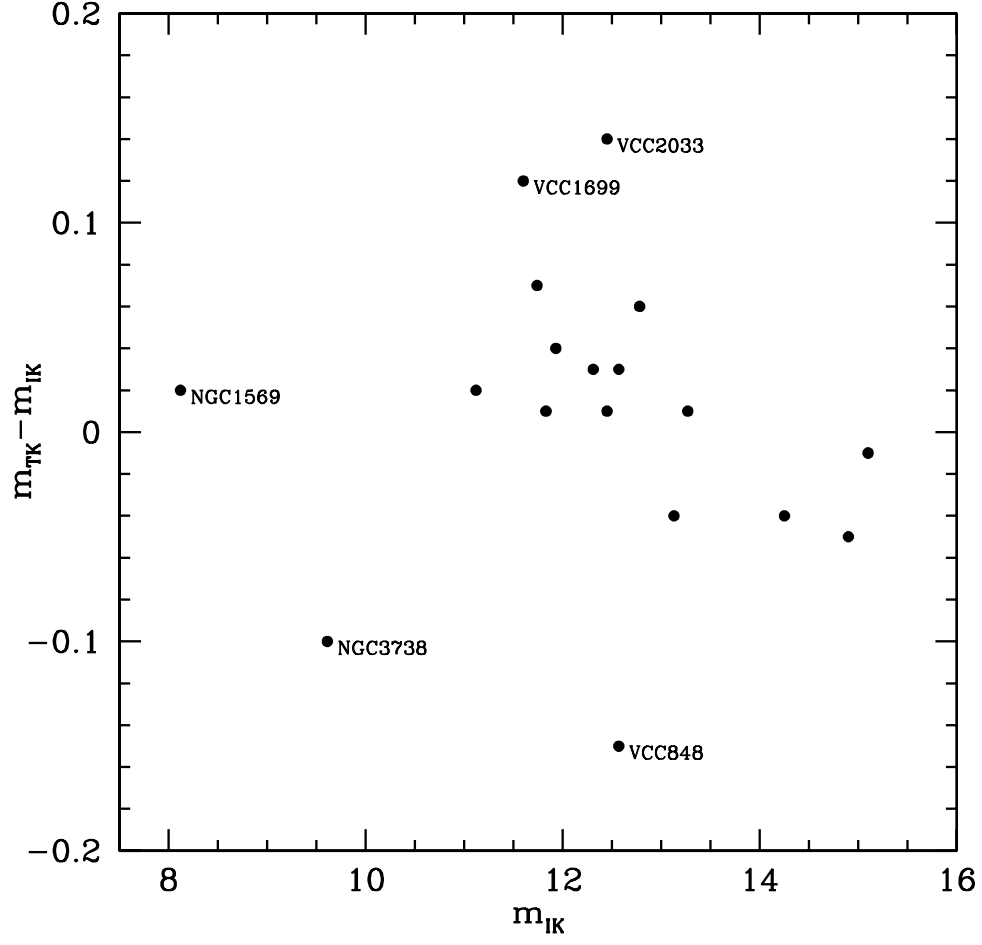


Fig. 2.— The difference between the apparent total magnitude  $m_T$  and the apparent isophotal magnitude  $m_I$  versus  $m_I$  for the  $K_s$  band. The three Virgo BCDs with residuals larger than 0.1 mag were all observed in poor weather.

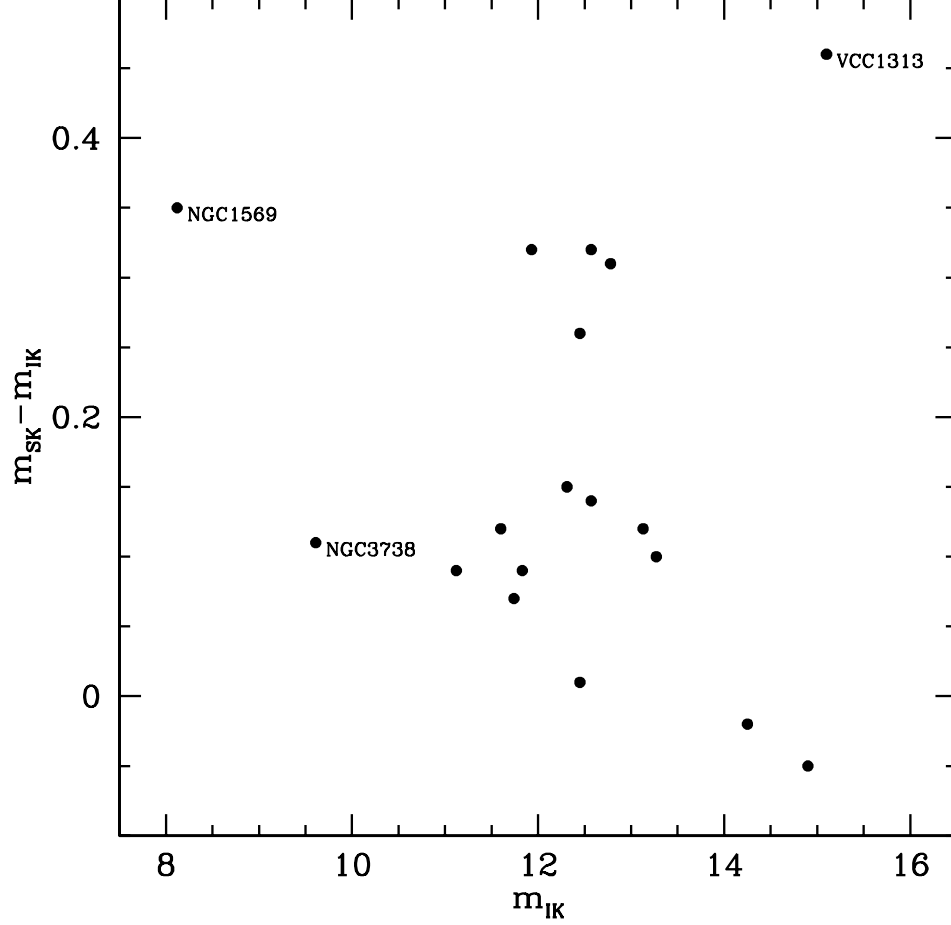


Fig. 3.— The difference between the apparent sech magnitude  $m_S$  and the apparent isophotal magnitude  $m_I$  versus  $m_I$  for the  $K_s$  band. The graph reveals the effect of starbursts on  $K_s$  magnitudes. VCC1313 has a very small size, which limited the number of samples for fitting.

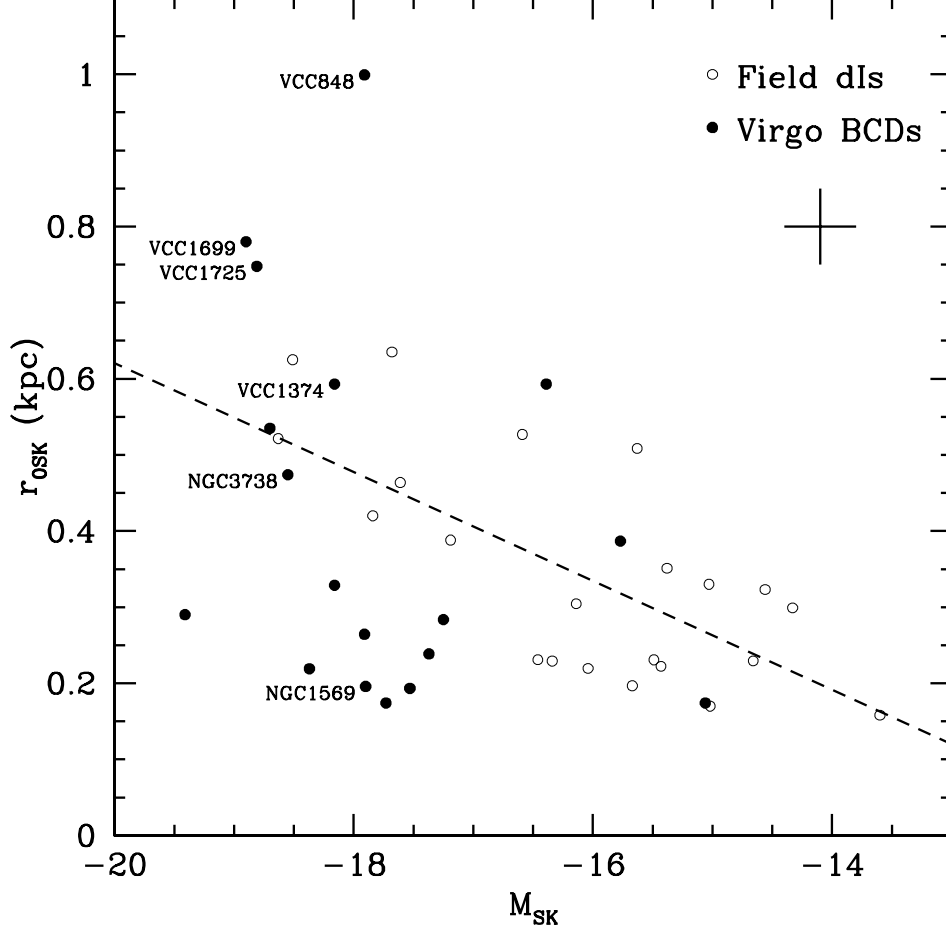


Fig. 4.— The scale length  $r_{0S}$  of the sech profile versus the absolute magnitude  $M_S$  of the sech component in  $K_s$ . BCDs and the two star burst dIs are represented as filled circles, and dIs from Paper I as open circles. The dashed line is a linear fit to the dIs alone. VCC 848 appears as an outlier, while VCC 1699, VCC 1725 and VCC 1374 were fitted using the sech component alone.

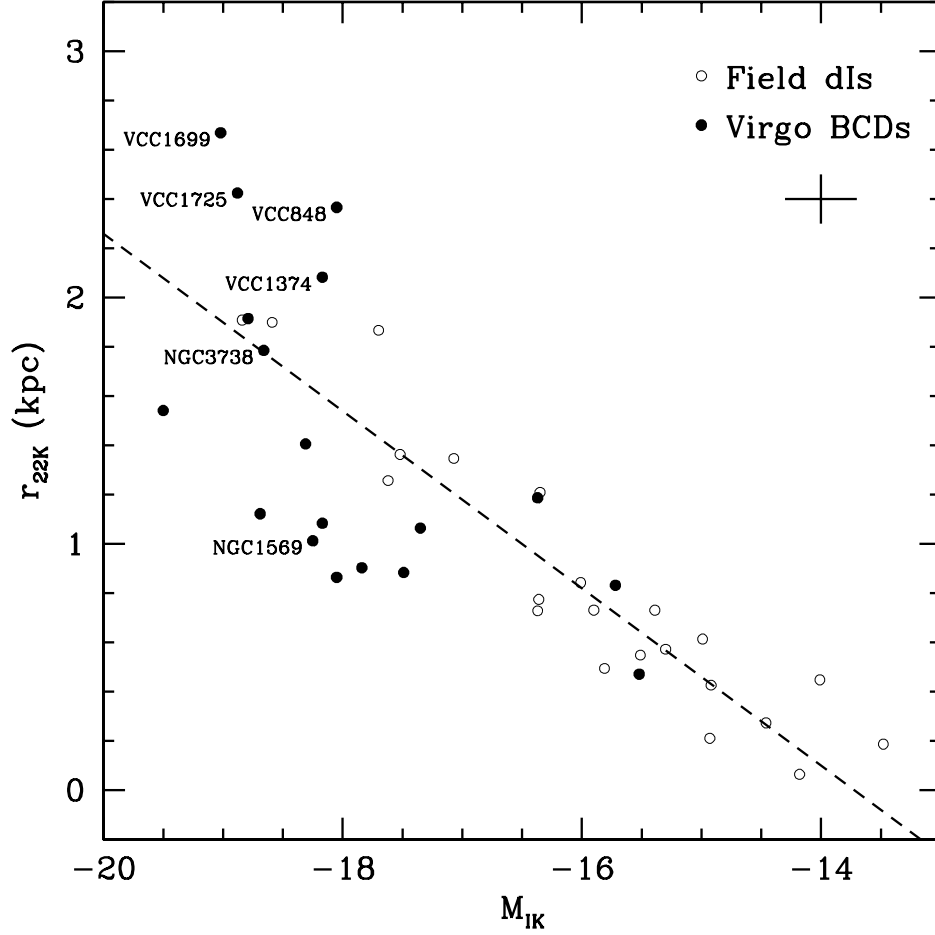


Fig. 5.— The semimajor axis  $r_{22}$  of the isophote  $K_S=22$  mag arcsec $^{-1}$  of the sech component, versus the absolute isophotal magnitude  $M_I$  in  $K_s$ . BCDs and the two star burst dIs are represented as filled circles, while dIs from Paper I as open circles. Two two starburst field galaxies, NGC 1569 and NGC 3738, are labeled. VCC 1699, VCC 1725, and VCC 1374 were all fitted with sech component alone. VCC 848 is an outlier observed in poor conditions. A linear fit to the dIs alone is shown as a dashed line.

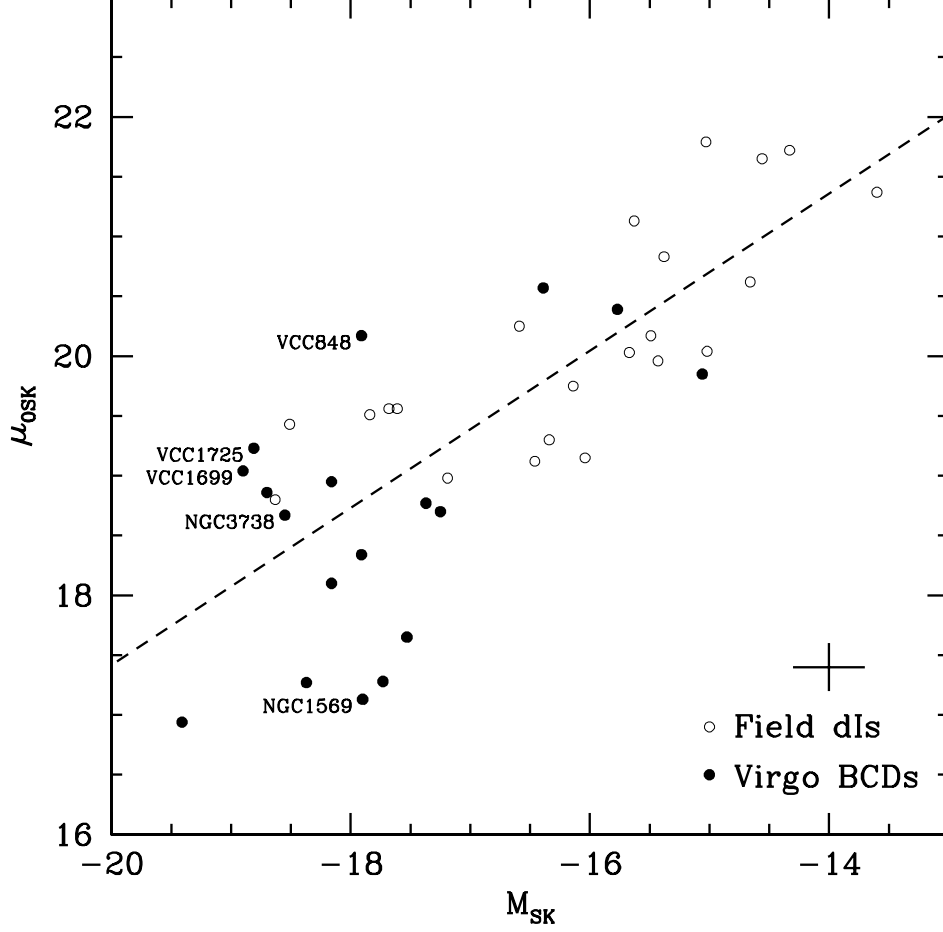


Fig. 6.— The sech central surface brightness  $\mu_{0S}$  versus the sech absolute magnitude  $M_S$  for the  $K_s$  band. BCDs and the two star burst dIs are plotted with filled circles, while dIs from Paper I with open circles. The two star burst dIs are labeled. VCC 848 is an outlier observed in poor weather, while VCC 1725 and VCC 1699 were fitted using sech component alone. A fit through the rest of the points (dIs and BCDs) is plotted as a dashed line.



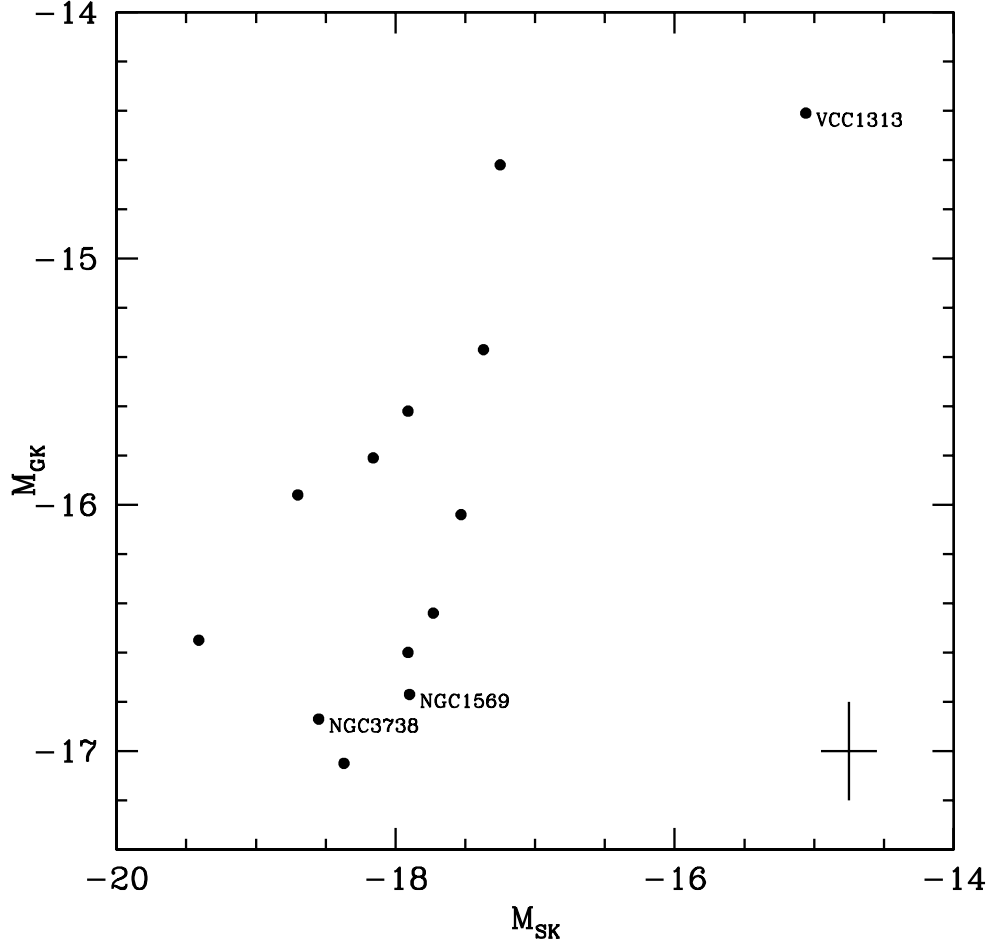


Fig. 7.— The Gaussian magnitude  $M_G$  versus the sech magnitude  $M_S$  for our BCD sample and two star burst dIs, in  $K_s$ . There is a rough correlation between the strength of the starburst and the luminosity of the diffuse component, in the sense that objects with brighter underlying components have more luminous bursts. VCC 1313’s position may well be the result of the poorer quality of the data available for it.

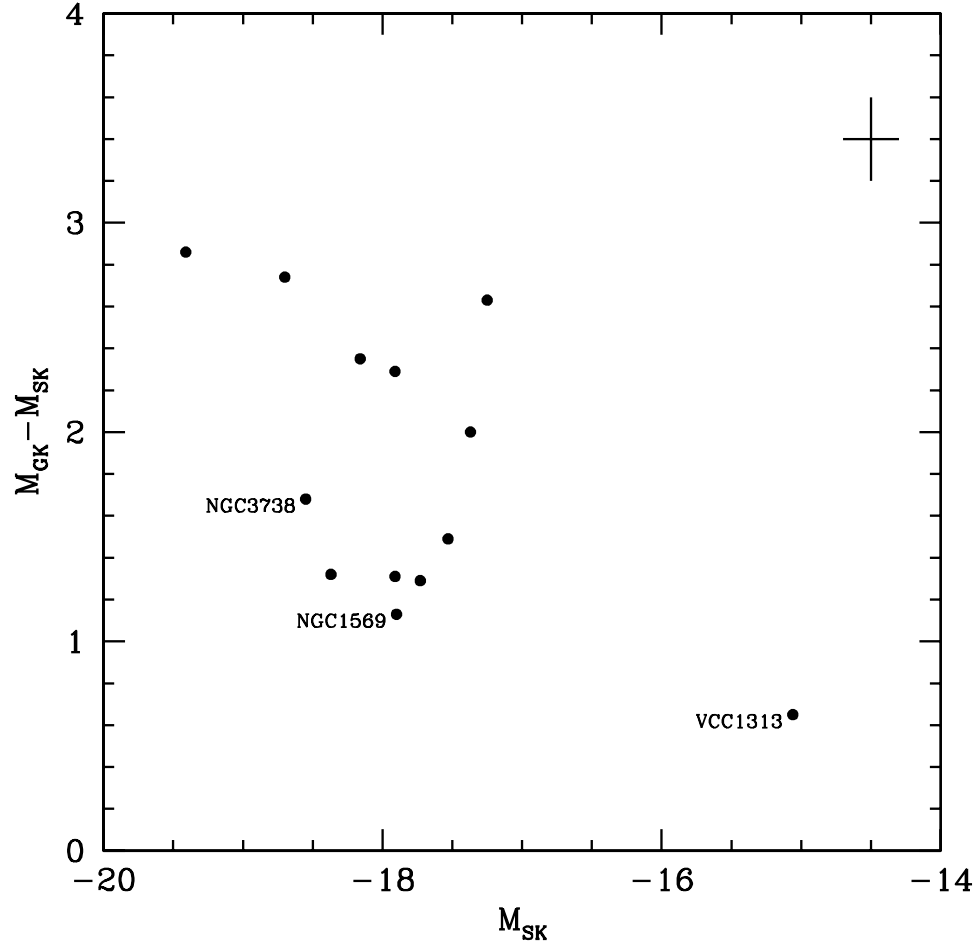


Fig. 8.—  $M_G - M_S$  versus  $M_S$ . There is no evidence that the relative strength of bursts grows with luminosity. VCC 1313 was observed in poor weather, being also a very compact object.

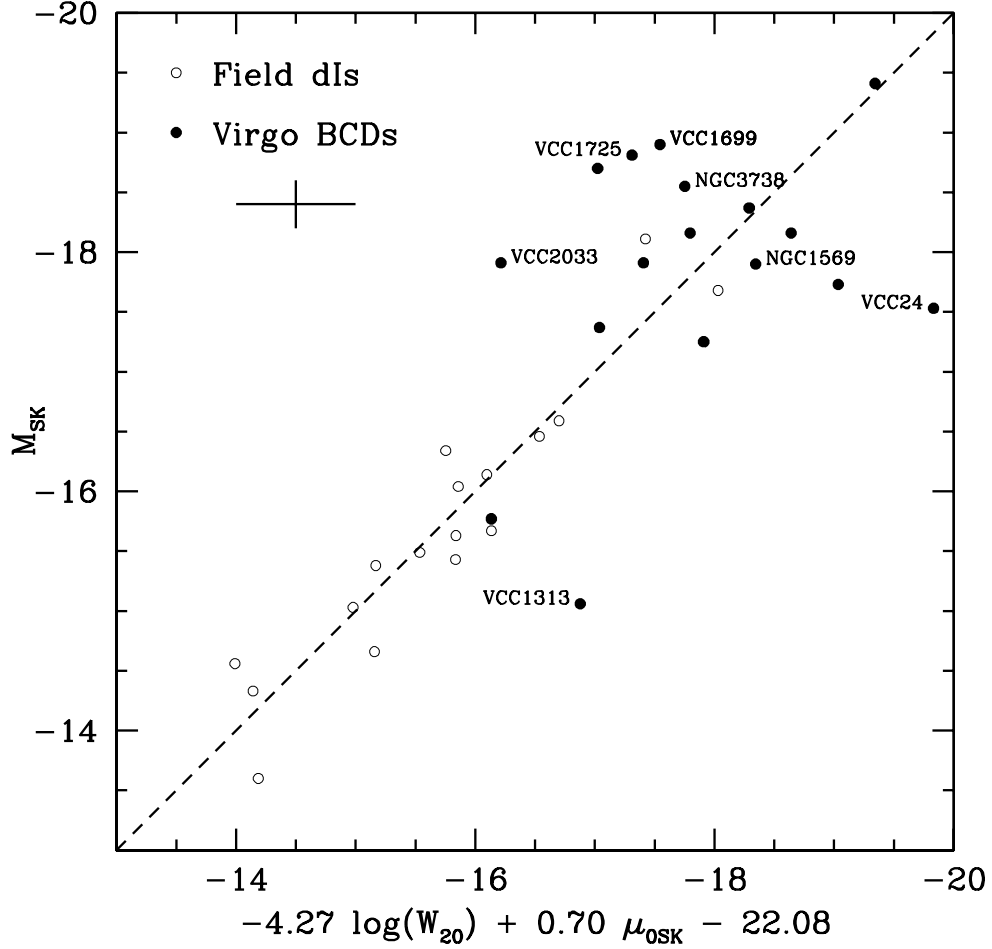


Fig. 9.— The dI fundamental plane in  $K_S$ , as described by the relation between the absolute sech magnitude  $M_S$ , HI line-width  $W_{20}$ , and the central sech surface brightness  $\mu_0$  (Paper I). dIs are represented by open circles, while BCDs and the two star burst dIs are marked by filled circles. The BCDs show more spread than the dIs, but they scatter around the same relation. The error bar in the X axis refers to average BCD data and is due mainly to uncertainties in  $W_{20}$ . NGC 1569 and NGC 3738 are labeled, along with the most deviant Virgo BCDs, which have the largest uncertainties in  $W_{20}$  (as high as 13 km/s, which translates into 4.5 mag in the first term of the FP).